Shaping SBA-15 particles into highly porous macro-mesoporous monoliths by digital light processing

Applied Materials Today 52 (2026) 103370

Contents lists available at ScienceDirect

Applied Materials Today

journal homepage: www.elsevier.com/locate/apmt

Shaping SBA-15 particles into highly porous macro-mesoporous monoliths by digital light processing

Sebastien Buys [a,1], Arianna Bertero [b,1], Corine Gérardin [a], Bartolomeo Coppola [b,*], Julien Schmitt [a,*]

[a] ICGM, Univ Montpellier, CNRS, ENSCM, Montpellier, France
[b] INSTM R.U PoliTO-LINCE Laboratory, Department of Applied Science and Technology, Politecnico di Torino, Turin 10129, Italy

ARTICLE INFO

Keywords:
Macro-mesoporous monolith
SBA-15
Digital Light Processing

ABSTRACT

This study presents a simple procedure to design macro-mesoporous monoliths using well-known SBA-15 particles mixed with a commercial photocurable resin and Disperbyk-103 as dispersant to form a printable slurry for digital light processing (DLP). SBA-15 mesoporous silica rods give their well-defined and well-ordered mesoporosity to the material, while DLP allows shaping the particles in a macroporous monolith, using as example the gyroid macroporosity. SBA-15 particles were characterised before printing using a combination of SEM, SAXS and N_2 sorption to characterise their shape, mesopore organisation and mesopore volume respectively. Several formulations, with different concentrations of SBA-15 (15–18 wt%) with and without the presence of additives (non-porous silica particles or calcium oxide), were tested. Rheological studies proved all formulations to have a shear-thinning behaviour, and only formulations with a viscosity at printing shear below 5 Pa.s were used for printing. First printing proved most formulations could be printed, but only the formulation with CaO as sintering aids gives a material that withstand calcination at 1000°C. Finally, the most suited formulation (15 wt% of SBA-15 in the total mixture; with 5 wt% of Disperbyk-103 and 1 wt% of CaO compared to SBA-15) was used to print "dense" cylinders, exhibiting only the SBA-15 mesoporosity and "macroporous" cylinders with a gyroidal macroporosity. The samples withstand sintering up to 1000°C without loss of the mesoporous organisation or an alteration of the shape of SBA-15 particles composing the monolith. This work hence shows a simple procedure to valorise SBA-15 particles into monoliths with hierarchical porosity, with possible applications as adsorbents or filters.

1. Introduction

Ordered mesoporous silicas (OMS), exhibiting a long-range ordered mesoporosity, are extensively studied since their discovery due to their high specific surface area, tailored pore structure and thermal stability [1,2]. Among them, SBA−15, obtained using Pluronic P123 as a structure directing agent and tetraethyl orthosilicate (TEOS) as the silica source, exhibits a well-defined 2D-hexagonal mesoporosity, with pore diameters in the range 5–10 nm [3,4], that makes it suitable for a wide range of applications, such as a support for heterogeneous catalysis [5,6], a carrier for drug delivery [7,8], or a filter for water [5] or air [9,10] depollution. Yet, the latter requires two conditions. First, a surface functionalisation of the silica is needed to enhance the adsorption of the targeted species. *Ko et al.* demonstrated that SBA−15 particles can be easily functionalised with amine groups, using (3-aminopropyl) trimethoxysilane (APTMS), [3-(methylamino)propyl] trimethoxysilane (MAPTMS), or [3-(diethylamino) propyl] trimethoxysilane (DEAPTMS) for grafting primary, secondary or tertiary amine groups respectively. They showed that the addition of amines imparts the material with CO_2 sorption capacity, with higher quantities adsorbed for the primary amines than for the secondary and above all tertiary amines [11]. Second, a processing step of the material into macro-mesoporous monoliths adapted to the application is necessary. Indeed, SBA−15 is usually synthesised as a powder [3,4], which induces strong limitations in its processability: powder bed systems exhibit poor manageability and recyclability, while inducing high pressure drops and low mass transfer rate under operation [12,13]. Another application that could benefit from the shaping of functional SBA−15 mesoporous silica particles into

* Corresponding authors.
E-mail addresses: bartolomeo.coppola@polito.it (B. Coppola), julien.schmitt@umontpellier.fr (J. Schmitt).
[1] Authors with equal contributions

https://doi.org/10.1016/j.apmt.2026.103370
Received 24 June 2026; Received in revised form 28 July 2026; Accepted 29 July 2026
Available online 5 August 2026

macroporous monoliths is oral delivery of drugs [8,14,15], including vaccines [16–18]. Indeed, more than 50% of currently marketed drugs are poorly soluble in water. Further, they often exhibit limited stability in body fluids, which makes the use of an inorganic carrier advantageous for an efficient oral administration, in order to survive the gastric environment and efficiently deliver the drug in the intestine. [19] SBA−15, with its low cytotoxicity and large mesopore volume, is a suitable candidate for such a carrier [16]. If the well-defined mesopores can encapsulate a large variety of small molecules, shaping the material into macro-mesoporous monoliths such as tablets would not only allow better patient compliance, but also favour the loading of larger molecules in the macropores and further facilitate diffusion and transport of the drugs for a controlled release of the compounds through the hierarchical porosity [19].

The most common synthesis processes of SBA−15 are the precipitation methods, that yield submicrometer-sized mesoporous particles [3,4]. The particles are formed by the cooperative templating mechanism (CTM) between micelles of P123 and silica oligomers in aqueous solution, that results in a phase separation and the formation of a hybrid 2D-hexagonal mesophase [20,21]. By careful control of the synthesis conditions, such as pH, temperature, stirring or choice of the structure directing agent, the morphology of the grains can be tailored: with rod-like, rice-shape, donuts-shaped or platelet-like particles, as evidenced in the literature [22–24]. The one-pot synthesis of purely mesoporous monoliths also exists in the literature, and is carried by mixing structure directing agent and silica source at high concentration [25–27], but the slow procedure spans over a week and requires the removal of the large amount of alcohol generated during the silica source hydrolysis. Further, the sample lacks a macroporosity required for the aforementioned applications. Scientists have managed to form hierarchically-porous monoliths by impregnation of SBA−15 particles onto a polymethylmethacrylate (PMMA) scaffold, followed by thermal treatments. The macroporosity is given by the imprint of the PMMA beads used to form the scaffold [28]. Alternatively, macro-mesoporous materials can be obtained by the combination of spinodal decomposition and sol-gel chemistry [29,30]. The spinodal decomposition of a mixture of polyethylene glycol and silica allows forming a macroporous material with a complex tortuosity, while the slow sol-gel condensation in the presence of cetyltrimethylammonium bromide (CTAB) as a porogen agent leads to a well-ordered mesoporosity. The procedure requires a long ageing step, that can take up to a week, while the smaller size of CTAB micelles compared to P123 used in SBA−15 gives small mesopores that limit the range of applications. Recently, *Kozakiewicz-Latała et al.* have used this procedure to form tablets for the delivery of Dexketoprofen, a nonsteroidal anti-inflammatory drug. They showed that the hierarchical macro-mesoporous architecture enabled better control of the drug release [19]. Finally, the pseudomorphic transformation of a priorly prepared macroporous silica scaffold can produce a monolith with hierarchical porosity [31]. Yet, the pseudomorphic transformation of silica into OMS, necessary to maintain the macrostructure, requires a fine control of the silica dissolution/reprecipitation parameters, and is hence not easily industrially scalable. Further, the spinodal decomposition does not allow to control the architecture of the macroporosity.

A promising approach to design a macro-mesoporous material with a completely tailored macroporous structure is the use of additive manufacturing (AM). AM, also called 3D-printing, is an umbrella term to describe different techniques that allow the design of the material layer-by-layer, by successive addition of matter. Several challenges, including poor resolution, surface quality, mechanical properties and scalability, slowed the implementation of AM in the ceramic fields compared to polymers or metals [32,33]. Recent years have seen a large progress in the shaping of ceramic-based materials. Notably, extrusion-based techniques (such as Direct Ink Writing or DIW) or stereolithography-based ones (such as Digital Light Processing or DLP) were shown to be perfectly adapted to shape several ceramic-based materials, such as silica, [34,35] alumina, [36,37] zirconia [38–40] or composites. [41]. The versatility of designs allowed by AM permits obtaining ceramic-based monoliths for several applications, ranging from the medical field (dental prosthetics, [42] bone implants [43]) to aerospace (aerospike nozzles [44], SiC optical mirrors [45]) and notably materials for the environment (sensors [46], carbon capture and storage systems [47]). Yet, to our knowledge, only a few studies on the shaping of mesoporous materials, and especially SBA−15, into monoliths by AM can be found in the literature. Indeed most works related to the design of hierarchically-porous materials by AM notably for adsorption applications have focused on metal-organic frameworks or zeolites, as those do not require surface modification [48]. Nonetheless, the thermal stability of OMS and their easy post-printing surface functionalisation make them suitable candidates for adsorbents designed by AM.

Shao et al. coated a 3D-printed ceramic monolith with SBA−16, another mesoporous silica [49]. *Schmidt et al.* printed hydrophilic films using a carboxymethyl cellulose hydrogel loaded with mesoporous silica to act as drug carriers [50], while *Robert at al.* printed poly(vinylidene fluoride-co-hexafluoropropylene) reinforced with SBA−15 to improve the ionic conductivity of the printed electrode [51]. Some examples of mesoporous monoliths designed by extrusion techniques can be found in the literature. *Chandrasekar et al.* mixed SBA−15 with bentonite (clay), methylcellulose and TEOS in water to form an extrudable paste. They showed the mechanical strength of the extrudates increases with the concentration of additives while the specific surface area and pore volume decrease due to a possible blocking of the pores [52]. Similarly, *Thakkar et al.* studied the shaping of a commercial porous silica, PD−09024 by DIW [53]. They designed a macroporous aminosilica adsorbent for CO_2 capture application, by mixing silica particles or amine-grafted silica particles, clay and methyl cellulose in water or methanol to produce the printing ink. Via DIW, they managed to give a grid-like macroporosity to the material.

DIW has a resolution limited by the diameter of the nozzle used for extrusion (typically 600–800 μm), which prevents the design of more complex macrostructures. On the other hand, in DLP, the nominal lateral spatial resolution is defined by the projected pixel size (that generally lies in the range of ~25–100 μm) at the build plane. We previously demonstrated that DLP could be used to design ceramic-based materials such as mullite with grid-like, Schwartz-primitive or even gyroid macroporosities [54,55]. The two latter are part of the triply periodic minimal surfaces (TPMS) class, which maximises the surface-to-volume ratio and are hence desirable for applications where high contact surfaces are required.

In this study, we explore the feasibility to shape macro-mesoporous materials using well-defined SBA−15 rod-like particles via DLP. We have focused on the formulation of the photopolymerisable ink loaded with SBA−15 rods, controlling the amount of mesoporous silica particles, but also the presence of additives, such as non-porous silica or calcium oxide as sintering aids. After optimising the formulation procedure, printing and sintering steps, we showed that DLP can be successfully used to print cylinders with and without extra macroporosity. In the latter case, a complex macropore geometry, using the gyroid triply periodic minimal surfaces, was successfully printed.

2. Materials and methods

2.1. Materials

For the synthesis of SBA−15 particles, Pluronic P123 ($EO_{20}PO_{70}EO_{20}$), tetraethyl orthosilicate (TEOS) and HCl 37% were purchased from Sigma-Aldrich and used as received. For slurry preparation, a commercial blank photocurable resin (ADMATEC Europe BV, The Netherlands), a silica-rich photocurable resin labelled S130 (72.58 wt% of SiO_2, ADMATEC Europe BV, The Netherlands), a dispersant (Disperbyk−103, BYK Chemie, Germany) and CaO particles as sintering aids (Labotech, France) were used.

2.2. SBA−15 synthesis

The synthesis of SBA−15 was performed following already established procedures [3,20]. Briefly, an aqueous solution of P123 at 2.5 wt % in HCl 1.6 M was prepared and put under stirring at 40°C. Then, TEOS was added, and the reaction mixture was kept under stirring for 5 min for TEOS hydrolysis. The synthesis ran at 40°C for 24 h, before a hydrothermal treatment at 80°C for 24 h, filtration and calcination at 450°C. The synthesis solution had the following molar composition: $HCl/H_2O/P123/TEOS = 6/200/0.017/1$.

2.3. Slurry preparation

The slurries were prepared by mixing the previously synthesised SBA−15 particles in the blank resin under mechanical stirring, using Disperbyk−103 (labelled Byk in this study), a wetting and dispersing additive, to ensure the dispersion of the mesoporous silica particles in the mixture. To determine the optimised formulation conditions, several slurries were prepared by adding either a small amount of the S130 resin or CaO particles in the preparation. Slurries were prepared as follows: blank resin and dispersant were firstly mixed using a mechanical stirrer for a few minutes before the slow addition of S130/CaO (if any) and then SBA−15 powder. The formulation was kept under stirring for ca. 30 min, before being homogenised for 1 h at 350 rpm using agate spheres (d = 5 mm) in a planetary miller (Fritsch Pulverisette, Fritsch GmbH, Germany). A minimal solid loading of 15 wt% in SBA−15 in the slurry was targeted while the amount of dispersant was at least 5% compared to the SBA−15 mass. Table 1 gives the different formulations studied. Once the best formulation was selected, the slurry for the fabrication of large samples was prepared following the same protocol, with the exception of the planetary milling that was done 3 times for 1 h, with 1 h of rest time between two milling steps. Further, for this formulation, CaO particles were ball-milled in ethanol (mass ratio CaO:ethanol 1:6) for 26 h and dried at 80°C overnight before use.

2.4. DLP printing

Each slurry was tested for printing using the Digital Light Processing (DLP)-based stereolithographic device (ADMAFLEX 130, ADMATEC Europe BV, The Netherlands). The slurry was applied onto a moving tape using a 125 μm doctor blade. To assess the curing depth, slurries were exposed to UV light for various durations, see Table S1, **SI**. The cured layers, arranged in a chessboard pattern, were cleaned with paper to remove any uncured slurry, and the thickness of each layer was measured using a digital micrometer. After conducting several tests, the curing parameters were optimised to achieve the best balance between high resolution, good adhesion, and uniformity of each layer. As a result, the layer thickness was set at 50 μm, with an exposure time of 2 s, a 30 s delay before exposure to allow air bubbles to escape the slurry and a LED power which varied from 20.24 to 23.18 mW/cm² depending on the formulation. Then, for each slurry, a first printing test made of ca. 30 layers (aiming for a typical thickness of ca. 1.5 mm) of a simple rectangular shape (dimensions 90 ×30 mm²) was carried out to characterise their printability. A transport foil speed of v= 30 mm/s was used, which associated to the e=125 μm doctor's blade corresponds to shear rates $\dot{\gamma}$ of 240 s^{-1} ($\dot{\gamma} = \frac{v}{e}$). Note that for comparison, printing tests of the S130 silica-rich commercial resin were also carried.

Table 1
SBA−15 slurries prepared in the blank resin. [a] wt% in the slurry; [b] wt% compared to the amount of SBA−15.

Slurry	SBA−15 (wt%)[a]	Byk (%)[b]	S130 (%)[b]	CaO (%)[b]
S01	15	5	-	-
S02	15	7	5	-
S03	18	20	5	-
S04	15	5	-	1
S05	15	8	5	1

Once the printing tests were carried out and the best formulation was selected, printing of several types of samples was conducted using further optimised printing conditions. Prismatic samples (nominal dimensions of ca. 15 ×5 ×5 mm) for dilatometric measurements, dense cylinders or porous cylinders for sorption studies (both with nominal diameter x height of ca. 7 ×5 mm) were designed using the AutoCAD (Autodesk, San Francisco, CA, USA) and MSLattice [56] software. Porous cylinders exhibit a Gyroid macroporosity, which represents ca. 70 vol% of the sample (Fig. S1, **SI**). Optimised printing parameters included a layer thickness of 50 μm, a 2 s exposure time, a printing speed of 20 mm/s and a UV power of 350‰ (corresponding to a LED power of 23.18 mW/cm²).

2.5. Post-printing treatment

After printing, the green bodies underwent a water debinding for 24 h at 30°C, in order to remove any uncured slurry. Samples were then left to dry for 24 h in a high humidity chamber, followed by 24 h in a dry chamber. The samples were then dried at 60°C overnight, before undergoing thermal debinding and sintering in air, using an electric furnace (Nabertherm LHT, Nabertherm GmbH, Lilienthal, Germany), giving the final sintered bodies. The detailed debinding and sintering process is presented in Fig. 1. The maximum sintering temperature was for most samples 1000°C for 1 h. For first printing tests made using S01, sintering was also performed at 1100°C.

2.6. Characterisation

SBA−15 particles and sintered bodies were characterised using scanning electron microscopy (SEM), small-angle x-ray scattering (SAXS), x-ray diffraction (XRD), N_2-sorption studies at 77 K to characterise the particle shapes (and organisation within the sintered bodies), the pore organisation, the amorphous nature of silica and the sorption isotherms respectively. SEM measurements were carried on a FESEM Hitachi S4000 or Hitachi S4800 (Hitachi, Japan). Powders or sintered bodies were deposited on a stub and platinum-sputtered prior to the measurement. SAXS measurements were carried out at room temperature on an Anton Paar SAXSpoint 5.0 using 1.5 mm quartz capillaries at a wavelength λ = 1.54 Å and a sample-detector distance D= 1.608 m, corresponding to the scattering vector range $0.01 \leq q \leq 1.9$ nm^{-1}. XRD patterns were measured using an Empyrean Series 3 (Malvern Panalytical, United Kingdom). Micromeritics TriStar 3000 analyzer was used for N_2-sorption measurements. Prior to measurements, samples

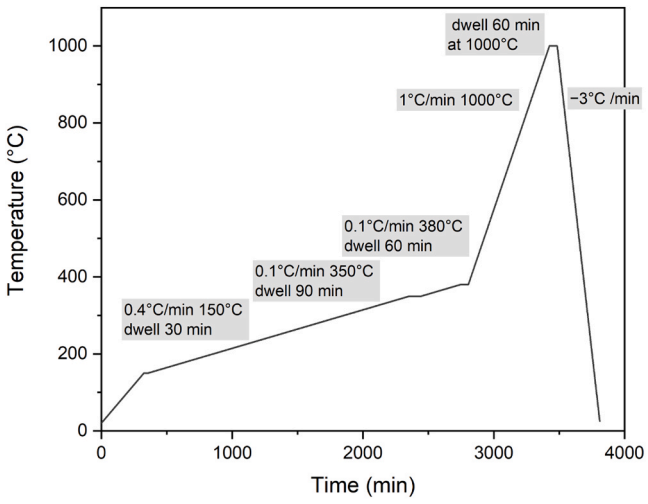

Fig. 1. Thermal debinding and sintering program.

were degassed at 280°C overnight. From N_2 sorption, information such as the specific surface area, micropore volume, mesopore volume and mesopore diameter was obtained via the BET and BJH models respectively. CaO particles were also studied via laser granulometry in ethanol (Mastersizer 3000, Malvern Pan'alytical, Worcestershire, UK) to measure their overall size in dispersion prior to use. Rheological studies were conducted on the different slurries, specifically the viscosity was determined as a function of the shear rate, using a rotational rheometer (Kinexus Pro+, Netzsch Geraetebau GmbH, Selb, Germany) equipped with stainless steel roughened parallel plates (20 mm diameter) with a 1 mm gap between plates. The densification behaviour was investigated by dilatometric analyses (Netzsch 402E, Germany), carried out up to 1000°C for 1 h, using the same thermal program reported in Fig. 1. Further, silica particles composing the S130 slurry were also characterised by SEM, XRD and N_2-sorption studies, after subjecting the slurry to the same thermal program in order to remove the organic compounds.

2.7. Density analysis

The geometrical density of the sintered bodies, ρ_{geo}, was calculated using mass and geometric measurements. The density of the sintered bodies was also determined using the buoyancy method, following Archimedes' principle (Density Determination Kit, Sartorius YDK01, Göttingen, Germany) and labelled ρ_{arch} (g/cm^3). These densities were compared to amorphous silica theoretical density (TD, 2.2 g.cm^{-3}), to obtain the relatives densities $\%\rho_{geo}$ and $\%\rho_{arch}$ respectively ($\%\rho = 100\rho/2.2$).

Both measurements allowed extracting the total porosity percentage ($P_{tot} = 100 - \%\rho_{geo}$) and the closed porosity percentage ($P_{close} = 100 - \%\rho_{arch}$) respectively, from which the open porosity percentage could be extracted ($P_{open} = P_{tot} - P_{close}$).

2.8. SAXS data analysis

Fitting of the SAXS data was made using a home-made software in Fortran, via a least-square fitting procedure [20,21]. A fitting model for a 2D-hexagonal mesoporous material was used and is presented in supplementary information. Briefly, the model depends on the following parameters: the lattice parameter a of the 2D-hexagonal network, the pore diameter D_p, the domain size D_m that characterises the extension of a 2D-hexagonal monodomain (all in nm), and two parameters that describe some disorder in the lattice: σ and σ_{DW} (both in %), that give the polydispersity in size and in positioning of the pores respectively.

3. Result and discussion

3.1. Silica powders characterisation

Prior to the slurry formulation, SBA−15 particles were characterised using SEM, SAXS and N_2 sorption in order to evidence their overall shape, pore organisation and pore volume respectively (Fig. 2). The amorphous silica material is shaped as submicrometric mesoporous rods of diameter x length = 1.1±0.2 × 0.22±0.02 µm (from the analysis of 50 particles on SEM micrographs), with a 2D-hexagonal pore organisation of lattice parameter a = 10.7±0.4 nm (from SAXS), pore diameter D = 7.5±0.6 nm (from BJH analysis). The sample exhibits a clear type I + IV isotherm in nitrogen sorption, characteristic of a microporous and mesoporous material, with respective microporous volume and mesoporous volume V_{micro} = 0.031±0.002 cm^3/g and V_{meso} = 0.55 ±0.04 cm^3/g, while the specific surface area obtained by the BET analysis is found at 656±11 m^2/g. The porous volume represents ca. 56% of the particle volume. For comparison, silica particles used in the commercial S130 were also characterised by XRD, and laser granulometry, by calcining the resin at 1000°C following the protocol described in Fig. 1. Results are presented in Fig. S2, **SI**. Similarly to SBA−15, S130 silica particles are made of amorphous silica as seen in

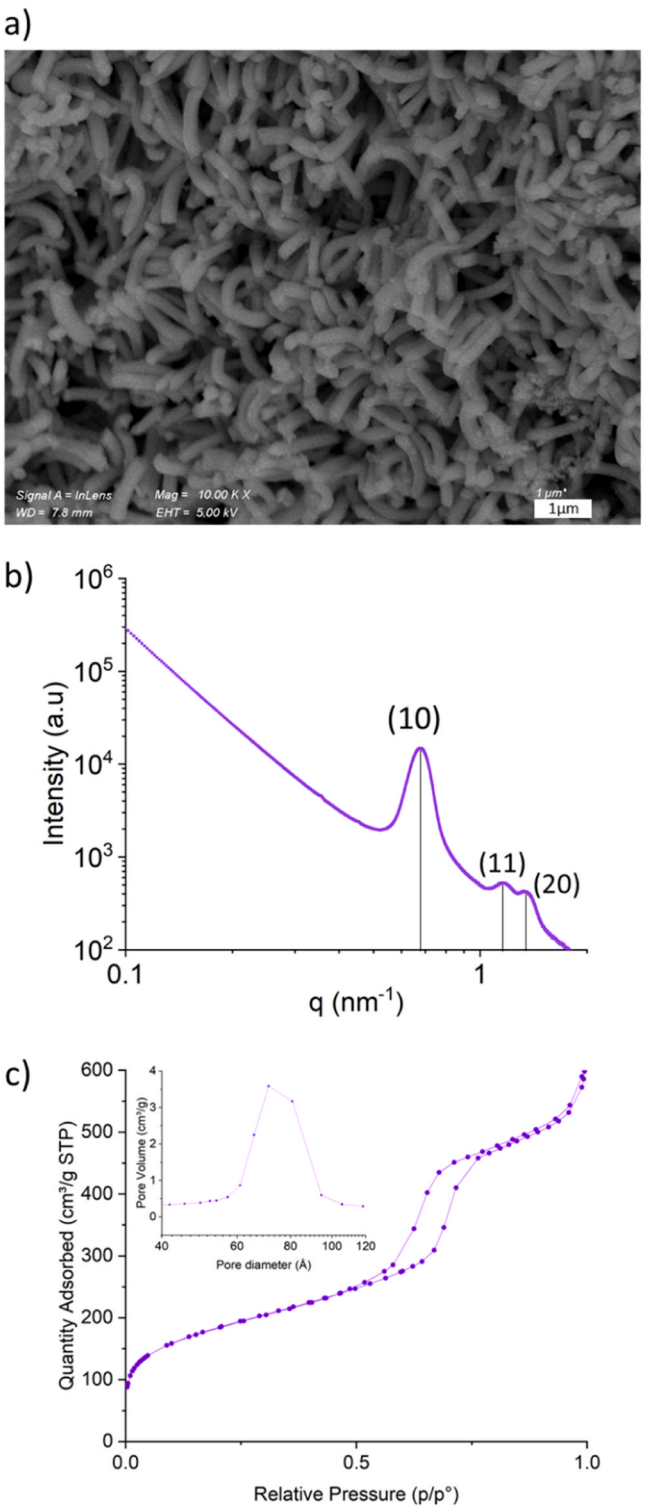

Fig. 2. (a) SEM micrograph, (b) SAXS pattern and (c) N_2-sorption isotherm of SBA−15 particles synthesised using P123 and TEOS at 40°C.

XRD, while their overall size in solution was found at D_{50} = 12.8 ±0.5 µm by laser granulometry. Yet they exhibit no porosity (specific surface area of 18±1 m^2/g) after calcination at 1000°C (Fig. S3, **SI**).

3.2. Rheological properties of the slurries

To ensure printability, all the slurry formulations were studied to evidence their rheological properties (Fig. 3). All slurries exhibit a shear-

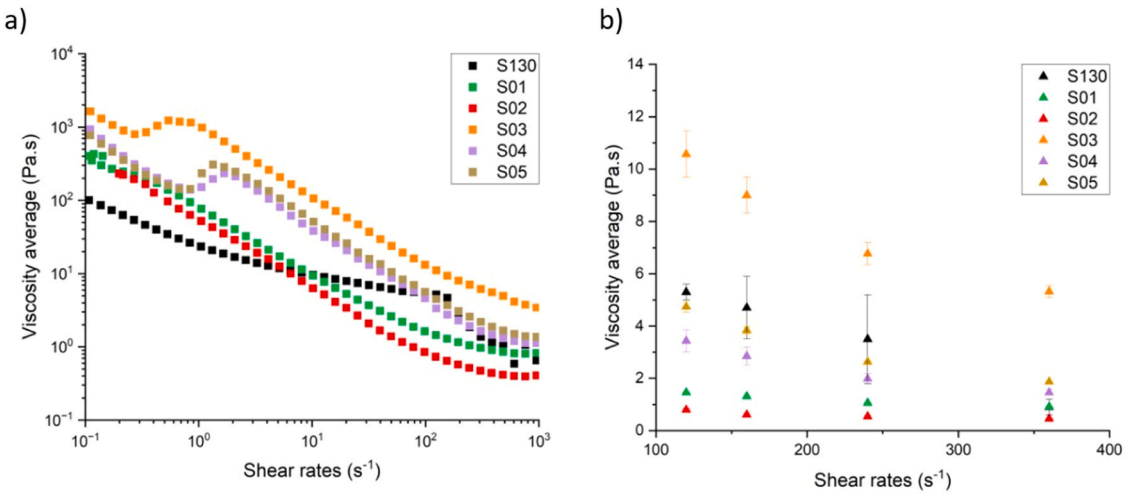

Fig. 3. Viscosity as a function of shear rates for the SBA−15 rich slurries (S01 to S05). For comparison, the commercial S130 resin, composed of amorphous silica particles, is also presented. (a) over the whole range of shear rates, (b) zoom on the range of shear rate used for printing.

thinning behaviour, mandatory to print samples using the DLP setup described in Materials and Methods. Comparatively to the S130 resin, a commercial slurry loaded with non-porous silica particles, S01–05 exhibits higher viscosity at low shear, yet, to the exception of S03, their viscosity at high shear rate is lower than S130. Specifically, the viscosity at printing shear rates (i.e. 240 s^{-1}) is found to be lower than 6 Pa.s for all samples except S03, which ensures the printability of the concerned formulations [57,58]. When comparing S01 and S02, the addition of a small fraction of the S130 resin in the SBA−15 slurry has little influence on the rheological properties but it does require a higher amount of dispersant to achieve a homogeneous dispersion (7% instead of 5% with respect to SBA−15 amount). 15 wt% of SBA−15 in the slurry is considered a maximum: indeed,

S03 (prepared with 18 wt% of SBA−15) requires a significantly higher amount of dispersant compared to S01 (20% instead of 7%) while exhibiting much higher viscosity profiles. Notably, its viscosity at printing shear rate, > 6 Pa.s, is deemed not acceptable for printing. It is important to note that, compared to S01, S03 exhibits a temporary increase of the viscosity at intermediate shear rates (ca. 1 s^{-1}), which may be due to a local orientation of the rods during the shear, as this rearrangement may induce friction between particles and temporarily increase the shear. Although 15 wt% of SBA−15 seems a low amount to obtain a printable slurry, due to the porous nature of SBA−15 (whose porosity represent ca. 56 vol% of one particle), this corresponds to particles occupying 20 vol% of the slurry. Finally, the addition of 1% CaO as a sintering aid (for S04 and S05) does increase slightly the viscosity of the formulations, and induces some interactions between CaO particles and rods that again increase the viscosity at intermediate shear rates, but the viscosity at high shear is kept within the printable range.

3.3. Sample porosity

All the formulations were tested for printing, except S03. After printing tests and sintering, rectangular samples obtained from every slurry with a printing speed of 30 mm/s were studied both in terms of geometrical and Archimedes densities, in order to extract the total (P_{tot}), closed (P_{close}) and open porosity (P_{open}) percentages in the materials (see Table 2). A sample made using the commercial silica-rich resin S130 was also prepared for comparison. Each formulation of SBA−15 particles exhibits a high level of open porosity, superior to 70%, even higher than the inner mesoporosity of the SBA−15 particles (56%). This can be explained by the addition of an inter-particle porosity from the shaping to the intra-particle mesoporosity observed in the powder. Indeed, the S130 sample also exhibits a high open porosity (reaching 30%),

Table 2
Porosity of the different samples printed at 30 mm/s after thermal debinding and sintering at 1000°C.

Samples	P_{tot} (%)	P_{close} (%)	P_{open} (%)
S130	40±10	4±1	36±10
S01	86±2	16±1	70±3
S02	85±4	1±5	84±9
S04	80±5	8±2	73±8
S05	83±4	12±2	71±6

although the slurry is composed of non-porous silica particles. This high inter-particle porosity is probably due to the low sintering temperature applied (1000°C), which prevents the complete fusing of the particles. Interestingly, adding a small amount of S130 to the SBA−15 slurry (S02) reduces the closed porosity, possibly as S130 are more reactive and can act as fillers between SBA−15 rods promoting small close pores disappearance or coalescence. The same phenomenon is observed when CaO is added (S04), which is known to sinter at lower temperature and react with silica to form mixed phases. Yet adding both S130 and CaO does not result in an even lower fraction of close porosity, suggesting that both additives have an antagonistic effect when combined. In any case, from the density measurements, neither S130 nor CaO induces a strong reduction of the open porosity, which we expect to be at least partially due to the mesoporosity of the SBA−15 particles composing the printed sample. To confirm this, these samples were also characterised via nitrogen-sorption.

3.4. Nitrogen sorption

Nitrogen sorption measurements were also performed on the sintered bodies to evaluate the stability of the mesoporosity of the rods after the printing and thermal treatments. The isotherms and BJH pore diameter distributions for all printed formulations are presented in Fig. 4, while the specific surface area (from BET), the pore size and pore volume (from BJH) are summarized in Table 3. For comparison, the sample printed with solely S130 was also studied (Fig. S3, **SI**).

Samples S01 and S02 exhibit very similar type IV isotherms, with well-defined hysteresis loops characteristic of mesoporous materials and similar to the isotherm observed for the SBA−15 powder. This indicates that the mesoporosity of the rods is mostly preserved after the printing and thermal debinding steps. Yet, the BET specific surface areas are decreased after shaping, with values of 271±10 m^2/g and 269±8 m^2/g, respectively, compared to 656±11 m^2/g of the SBA−15 particles before

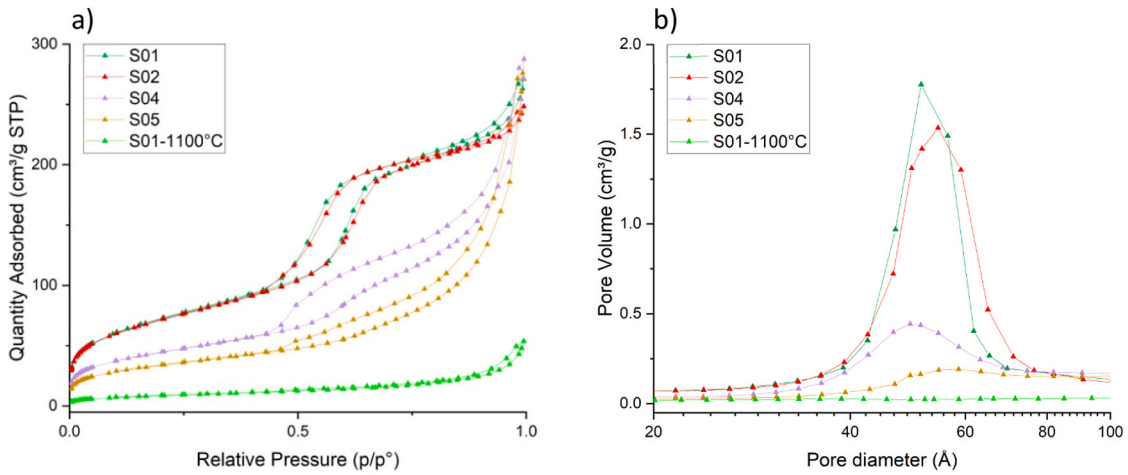

Fig. 4. (a) N_2-sorption isotherm, (b) BJH distribution of printed and sintered (at 1000°C) samples made from S01, S02, S04 and S05. For comparison, sample made with S01 and sintered at 1100°C is also given.

Table 3
Key results from N_2-sorption measurements for the printed samples with different slurry formulations.

Samples	S_{bet} (m^2/g)	D (nm)	$V_{mesopores}$ (cm^3/ g)	$V_{micropores}$ (cm^3/ g)
S130	18±1	-	-	-
S01	271±10	5.3±0.3	0.24±0.02	0.013±0.003
S02	269±8	5.4±0.5	0.24±0.02	0.015±0.003
S04	160±2	5.0±0.4	0.15±0.03	0.002±0.001
S05	118±4	5.7±1.0	0.10±0.03	0.002±0.001

printing. This is accompanied by a decrease of the pore diameter from 7.5±0.6 to 5.3±0.3 nm between the SBA−15 powder and S01, and of both the mesopore and micropore volume (V_{micro} = 0.031±0.002 and V_{meso} = 0.55±0.04 cm^3/g for SBA−15 powder versus V_{micro} = 0.013 ±0.003 and V_{meso} = 0.24±0.02 for cm^3/g for S01). This decrease is consistent with the sintering at 1000°C that compacts the structure. The presence of calcium oxide in samples S04 and S05 appears to significantly reduce the initial mesoporosity of the rods. This reduction is reflected in the BET surface areas, found at 160±2 m^2/g and 118±4 m^2/g, respectively. Yet, for S04, the total mesopore volume is not too decreased (from 0.24±0.02 to 0.15±0.03 cm^3 compared to S01) and the pore diameter remains similar (ca. 5 nm), which proves mesopores are still present and accessible, while micropores are almost completely lost (0.002±0.001 cm^3/g). For S05 on the other hand, the drastic decrease of the mesopore volume (to 0.10±0.03 cm^3/g) indicates that mesopores are not accessible or are significantly lost with this formulation. CaO is known to be a fluxing agent, which can decrease the sintering temperature of silica or form vitreous calcium silicate species. In the presence of non-porous S130, this effect seems worse, and this formulation seems not adequate for further use. Yet, without S130, although the specific surface area is lowered, mesopores are still clearly visible, and the sintering effect of CaO can improve the handling of the monolith, by partially fusing particles.

Nitrogen sorption measurements were also performed on sample S01 after sintering at 1100 °C. The results show a clear and complete collapse of the mesoporosity, with specific surface area falling at 29 m^2/g, indicating that 1100 °C is already too high for preserving the porous structure of the rods. The results from N_2-sorption measurements clearly demonstrate that the mesoporosity of the SBA−15 particles is maintained up to 1000°C, albeit with a reduction of the mesopore size and volume. Yet the porosity measurements showed a remarkably high open porosity for all formulations (≥70%). This further confirms the high contribution of the pores formed between particles during printing to the overall porosity of the macroscopic samples. This inter-particle extra porosity can help mitigate the reduction in specific surface area of the SBA−15 rods due to the sintering at 1000°C, by making a full use of the external surface of the particles that compose the material.

3.5. SAXS

This mesoporosity observed in N_2 sorption can be related to the mesopore organisation determined via SAXS. Indeed, all samples still exhibit a 2D-hexagonal mesopore organisation after printing and sintering at 1000°C (Fig. 5). SAXS patterns from S01 and S02 clearly show three Bragg peaks, associated to the (10), (11) and (20) planes of the 2D-hexagonal mesophase [20]. Table S2**, SI**, gives the position in q of each Bragg peak for all samples, from which the centre-to-centre distance between two pores $d_{c\text{-}c}$ and the lattice parameter a can be calculated. It should be noted that sintering does induce a clear shrinkage of the mesophase, with a lattice parameter that goes from a = 10.7±0.4 nm for the SBA−15 powder to a = 9.3±0.2 nm after shaping and sintering. The addition of CaO only partially affects the mesopore organisation, seen by a broadening of the peaks' width, in agreement with its role as fluxing

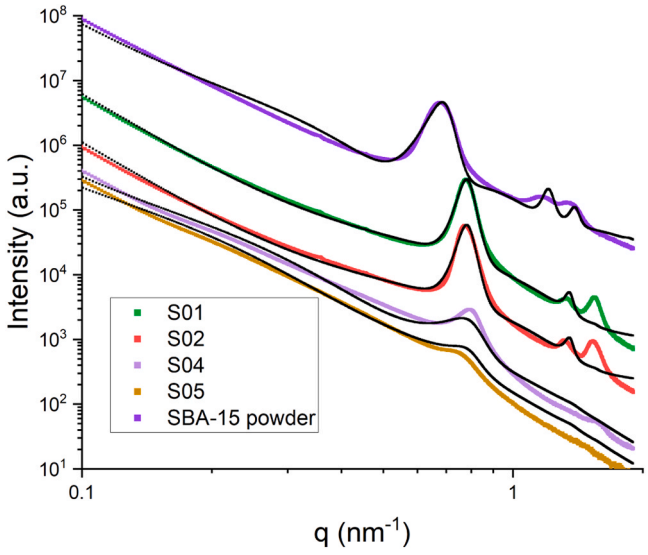

Fig. 5. SAXS patterns of printed and sintered (at 1000°C) samples made from S01, S02, S04 and S05. SBA−15 powder (non-sintered) is added for comparison. In black, the fits obtained using the model for mesoporous materials are given.

agent, but without deteriorating it completely. For S05, this phenomenon is again more pronounced, with (11) and (20) peaks being non-visible.

To further quantify this phenomenon, data were fitted using the model of a 2D-hexagonal mesoporous network described in SI (black lines in Fig. 5). The fits reproduce well the 2D-hexagonal organisation and notably the (10) peak, yet some divergences for the (11) and (20) peaks can be observed, which is expected by the use of a simplified model for describing the pores. More complex models, such as those incorporating smearing at the interface between pores and silica walls or a less dense silica shell were not considered to avoid over-parameterization. Yet the results from the fits allow drawing some clear conclusions on the effect of additive manufacturing, presence of additives and sintering on the 2D-hexagonal porosity. For the SBA−15 powder that was only calcined at 600°C, fitting gave a lattice parameter $a = 10.4\pm0.1$ nm consistent with the calculation from the Bragg peaks position, associated to a domain size $D_m = 103\pm5$ nm, and low indices of disorder, with $\sigma = 20\pm2\%$ and $\sigma_{DW} = 4\pm1\%$, all of which show a well-defined mesostructure with large domains. Notably, the polydispersity in size σ is consistent with the ones from the P123 micelles used to template the mesopores [59]. The pore diameter, D_p is found at 8.2 ±0.1 nm, which is in large agreement with the N_2-sorption results (7.5 ±0.6 nm). Results for S01 and S02 are highly similar, with a lattice parameter that shrinks to $a = 9.3\pm0.1$ nm due to the sintering at 1000°C without deteriorating the domain size D_m found at 128±5 nm for S01. This shrinkage in lattice parameter induces a shrinkage of the pore diameter $D_p = 4.6\pm0.1$ nm, found slightly smaller than in N_2 sorption. The difference may be due to the addition of the polydispersity in size in SAXS fitting, again found at ca. 20%. Sintering up to 1000°C seems to induce some positioning disorder as can be seen from the increase of σ_{DW} to ca. 8%. The addition of CaO does significantly alter the quality of the mesostructure, as seen with S04. Indeed, both the domain size and polydispersity in size of the pores strongly increase for this sample, suggesting both less well-defined pores and more defects in the mesostructure. These results are again consistent with nitrogen sorption and with the known effect of calcium oxide on silica sintering [60]. All the results from the fits are given in Table 4.

3.6. SEM

Finally, to evidence the influence of the process on the shape of the particle and study a possible orientation of the rods in the monolith by the shearing induced during printing, SEM micrographs of the sintered bodies were taken (Fig. 6). The initial length of the rods is approximately 1.1±0.2 μm, and the width is 0.22±0.02 μm (see Fig. 1), measured on around 50 rods. After printing, the morphology of the rods remains unchanged whatever the slurry used, with similar dimensions: 1.0 ±0.2 μm in length and 0.18±0.04 μm in width for S01, used as example. SEM micrographs of samples printed using S04, that contains CaO compared to S01 (Table 1), are reported in Fig. 6 **e-f**. Micrographs show clear inclusions of CaO around the particles (highlighted in red circles in Fig. 6) that acts as a glue to maintain the structure, although the rod-like morphology of the particles is still visible. The same phenomenon is visible S05, where, due to the further addition of S130, the rod-like morphology of the starting material is barely visible. One could expect that the shear induced by the printing method would align the silica rods within the final sample. However, no visible alignment of the rods was observed for these samples. Possible explanations for this phenomenon are that the concentration of rods in the slurry was too low to favour alignment, the shear imparted during the spreading of the slurry was not high enough or the blade window was too large (i.e. 125 μm). Yet, SEM micrographs show some clear holes between the disordered rods, giving the previously discussed inter-particle porosity.

Overall, the rods can be processed using this printing technique while preserving their morphology and mesoporosity. The addition of small fraction of S130 commercial resin, including non-porous silica particles, had little effect on the investigated properties (either N_2 sorption, or SAXS) or organisation within the materials (with little differences in SEM micrographs), nor did it allow a better processability. After printing and sintering at 1000°C, these samples are highly fragile and easily breakable just by manipulation. For this reason, and although it induces a reduction of the accessible mesoporosity, bulk 3D samples were then printed using solely formulation S04, to use CaO as a sintering aid to render the structure more robust.

Table 4
Results from the fitting of the SAXS data using the model described in supplementary information. a, D_m and D_p are given in nm, while σ and σ_{DW} are given in %. For S05, the weak Bragg peak remaining forced to fix some parameters (given in italic).

Samples	a (±0.1)	D_m (±5)	D_p (±0.1)	σ (±2)	σ_{DW} (±1)
SBA−15 powder	10.4	103	8.2	20	4
S01	9.3	128	4.6	20	8
S02	9.2	125	4.6	19	8
S04	9.0	55	5.4	62	3
S05	9.1	*55*	5.4	*80*	4
Cylinder	9.3	105	6.8	28	13

3.7. Fully printed dense and macroporous samples

After investigating different formulation conditions, bulk samples were 3D printed using S04, then sintered using the thermal treatment presented in Fig. 1. CaO was previously ball- milled to reduce the size of the particles from $D_{50} = 9.04\pm0.05$ μm to 1.91 ± 0.05 μm after 26 h of ball-milling (see Fig. S4**, SI**). Two types of samples were printed, dense cylinders and macroporous gyroids (see Fig. 7**.a,b**, and Fig. S5**, SI**). Sintering induced a shrinkage of ca. 22% for both the diameter and the overall height of the cylinders and gyroids, while the density of the samples is 89%TD (average of 3 measurements). This was further studied via dilatometric measurements on a printed barrette (Fig. 7**.c**). The sample experiences an overall shrinkage of ca. 27% during the whole thermal treatment process, consistent with the overall shrinkage observed for the two shapes studied. Two different shrinkage temperatures are observed. A first shrinkage starts at ca. 200°C and is reasonably due to the removal of the sacrificial resin. Then, a slower shrinkage initiates at ca. 600°C, probably associated to the sintering of CaO, and continues up to 1000°C. Let us note that this shrinkage continues during the one-hour dwell-time at 1000°C, which suggests that both sintering temperature and dwelling time could be adapted in the future to tailor the sintering state of the samples and hence both their structural and mechanical properties.

Both sintered morphologies were studied using N_2 sorption, and exhibit the similar type I + IV isotherm characteristic from micro and mesoporous materials (Fig. 7**.d**) as for the tests presented in Fig. 4. Notably, it is clear from the isotherms at high relative pressure that a higher meso/macroporosity is present in the samples, probably an inter-particle porosity. Analysis of the isotherms gives both a higher specific surface area and mesopore volumes for the macroporous sample (Gyroid) than for the non-macroporous (Cylinder), which indicates that the macroporosity, on top of being desirable for the use of such materials in flow applications, allows for an improved accessibility to the mesopores of the SBA−15 silica rods (Table 5). Let us note that the pore diameter D is found higher than in our previous tests (ca. 6.3 nm for both cylinder and gyroid compared to 5.5 nm above), explained by the use of a new batch of particles. One non macroporous cylinder was then crushed to be probed by SAXS, and results prove the mesopore organisation is well kept in the material even after complete printing, resin removal by thermal treatment and CaO/SBA−15 sintering at 1000°C (Fig. 7**.e**). Notably, the (11) and (20) peaks are still visible in this sample. This is reflected by the fitting, where the domain size is maintained at ca. 100 nm for this sample, albeit with higher disorder indices ($\sigma = 28\%$ and $\sigma_{DW}=13\%$) compared to the powder before shaping, and a

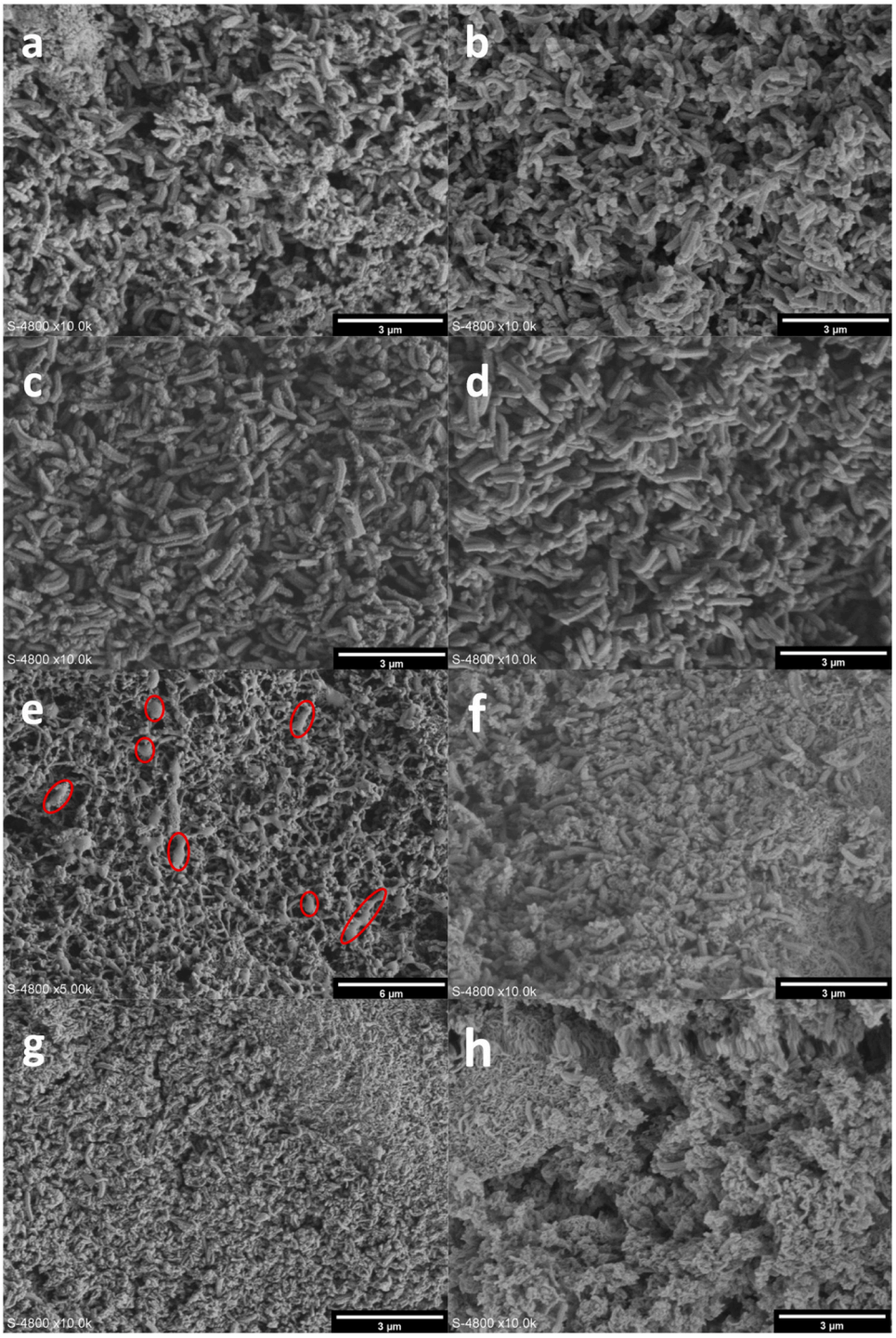

Fig. 6. SEM micrographs of surfaces either (a,c,e,g) parallel or (b,d,f,h) perpendicular to the foil transport, of samples printed using (a, b) S01; (c, d) S02; (e, f) S04; (g, h) S05.

pore diameter D_p in agreement with N_2-sorption results (Table 4). These improved textural properties compared to the previous test could be due to the ball-milling of CaO into smaller particles, ensuring an improved dispersion of the sintering aid. Similarly, SEM micrographs of fractured cylinders (Fig. 7**.f** and Fig. S6, **SI**) and gyroid (Fig. S6, **SI**) prove the morphology of the SBA−15 is well-maintained within the monolith. These monoliths can be handled easily without signs of breaking, and these results show great promises for their use as adsorbents for gas or water depollution, or as carriers for drug delivery.

Macro-mesoporous silica monoliths can be functionalised using an amine precursor such as (3-Aminopropyl) trimethoxysilane (APTMS), either by reaction in the liquid phase [61] or in the gas [62] phase. In the former approach, monoliths prepared by combining spinodal decomposition and sol-gel synthesis and calcined at 600°C were functionalised via a solvothermal procedure in toluene for 24 h, before vacuum filtration and air drying. They showed that the grafting ratio could be controlled by the amount of amine precursor added in the reaction mixture and that monoliths showed high CO_2 sorption properties (108 $mg.g^{-1}$ at 1 bar and 45°C), with an uptake stable for at least 5 cycles and up to 20 cycles. In the latter, APTMS vaporization was carried

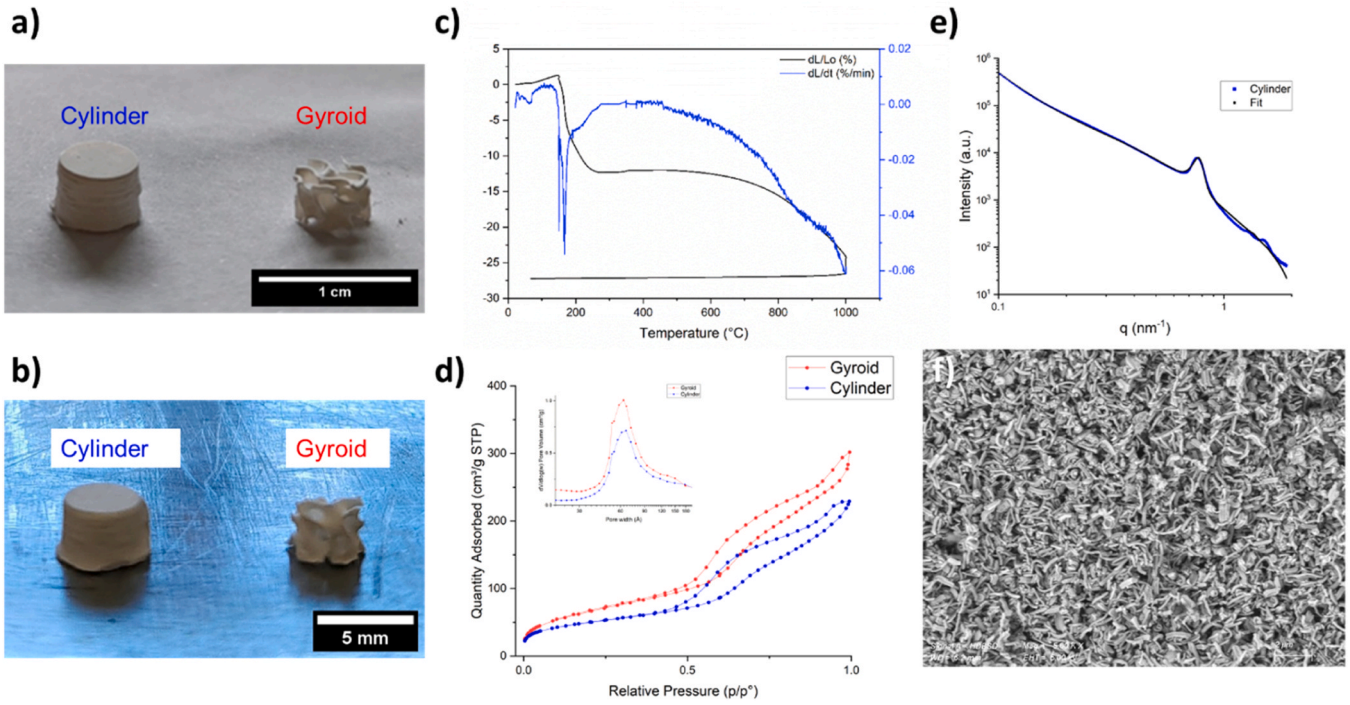

Fig. 7. Results from the "bulk" printed samples made using S04. (a,b) Photograph of both types of printed objects either (a) before or (b) after sintering, (c) dilatometry measurements of a printed prismatic sample, (d) N_2-sorption isotherms of both cylinder and gyroid, with the pore size from BJH analysis, (e) SAXS pattern of a grinded cylinder and its associated fit in black and (f) SEM micrograph from the fractured surface of a cylinder.

Table 5
Results from N_2-sorption isotherms of printed mesoporous samples.

Samples	S_{bet} (m^2/g)	D (nm)	$V_{mesopores}$ (cm^3/ g)	$V_{micropores}$ (cm^3/ g)
Gyroid	244±8	6.3±0.4	0.32±0.02	0.07±0.04
Cylinder	180±2	6.4±0.6	0.25±0.4	0.05±0.02

at 120°C for 24 h on the monolith before N_2 fluxing in order to remove any unreacted species. They found CO_2 sorption capacities similar to functionalised SBA−15 powder with a 36-fold lower pressure drop. With our technique, we can now tune the architecture of the macroporous network. Future work will focus on studying how this organisation can influence the functionalisation procedure, the CO_2-sorption capacities (notably in terms of mesopore accessibility and of cyclability) and the operating conditions when working in flow processes (pressure drops, breakthrough curves) [47].

4. Conclusion

In this paper, we have studied the design of macro-mesoporous silica materials by DLP. We have synthesised mesoporous SBA−15 silica rods that were characterised by SEM, N_2 sorption and SAXS and that exhibit a typical rod-like shape for the particles, with an inner 2D-hexagonal mesoporosity, with pore size at ca. 7.5 nm. These particles were mixed with a commercial photocurable resin at different concentrations (15–18 wt%) or in the presence of additives (a commercial silica-rich resin and/or CaO particles) to produce inks for DLP. We have studied the rheological properties of the inks in order to select the ones that were printable, and studied the printed and sintered samples using a combination of Archimedes' density measurements, SEM, SAXS and N_2 sorption. We have notably demonstrated that the samples can be sintered up to 1000°C, and that the presence of non-porous silica does not affect significantly the mesostructure but does not help the sintering process. Addition of CaO as a sintering aid, known to decrease the sintering temperature of silica, can still be employed up to 1000°C without a loss of the mesopore order, albeit a decrease of the mesopore volume (from 0.24 without to 0.17 cm^3/g with 1 wt% CaO). As samples with CaO were slightly less brittle, we used this formulation to design cylindrical monoliths, either purely mesoporous or adding a gyroidal macroporosity. Both structures were printable, the effect of sintering was monitored using dilatometric measurements while the sintered samples were characterised in N_2 sorption, SAXS and SEM. Dilatometry measurements indicate an initiation of sintering at ca. 600°C, consistent with the addition of CaO, with a more pronounced shrinkage starting at ca. 800°C. The final sintered samples exhibit a shrinkage of ca. 27% in the three dimensions. After sintering, the shape of the mesoporous rods and their inner mesopore organisation were maintained after printing and sintering, while the mesopore volume was found higher for the sample with the gyroid macroporosity (0.32 versus 0.25 cm^3/g for the non macroporous cylinder), suggesting that the macroporosity allows a better accessibility of the material without hindering its manageability. These results are a valid proof-of-concept that mesoporous particles such as SBA−15 can be shaped as macro-mesoporous monoliths using digital light processing, for possible applications in water or gas filtration, or as carriers for controlled drug delivery.

CRediT authorship contribution statement

Sebastien Buys: Writing – original draft, Methodology, Investigation, Formal analysis. **Arianna Bertero:** Writing – review & editing, Methodology, Investigation, Formal analysis. **Corine Gérardin:** Writing – review & editing, Supervision, Methodology, Formal analysis. **Bartolomeo Coppola:** Writing – review & editing, Supervision, Methodology, Funding acquisition, Formal analysis, Conceptualization. **Julien Schmitt:** Writing – original draft, Supervision, Methodology, Funding acquisition, Formal analysis, Conceptualization.

Declaration of Competing Interest

The authors declare that they have no known competing financial interests or personal relationships that could have appeared to influence

the work reported in this paper.

Acknowledgements

The authors acknowledge Bertrand Rebière for the SEM analyses and Arie Von der Lee (Institut Européen des Membranes) for the SAXS analysis. Mr Sébastien Buys thanks the Université de Montpellier and Ecole Doctorale Sciences Chimiques Balard for the PhD funding. This research was carried out thanks to the financial support of CNRS International Emerging Actions within the framework of the AMOUR project.

Appendix A. Supporting information

Supplementary data associated with this article can be found in the online version at doi:10.1016/j.apmt.2026.103370.

Data availability

Data will be made available on request.

References

[1] J.S. Beck, J.C. Vartuli, W.J. Roth, M.E. Leonowicz, C.T. Kresge, K.D. Schmitt, C.T. W. Chu, D.H. Olson, E.W. Sheppard, S.B. McCullen, J.B. Higgins, J.L. Schlenker, A new family of mesoporous molecular sieves prepared with liquid crystal templates, J. Am. Chem. Soc. 114 (27) (1992) 10834–10843, https://doi.org/10.1021/ja00053a020.

[2] C.T. Kresge, M.E. Leonowicz, W.J. Roth, J.C. Vartuli, J.S. Beck, Ordered mesoporous molecular sieves synthesized by a liquid-crystal template mechanism, Nature 359 (6397) (1992) 710–712, https://doi.org/10.1038/359710a0.

[3] D. Zhao, J. Feng, Q. Huo, N. Melosh, G.H. Fredrickson, B.F. Chmelka, G.D. Stucky, Triblock copolymer syntheses of mesoporous silica with periodic 50–300 angstrom pores, Science 279 (5350) (1998) 548–552, https://doi.org/10.1126/science.279.5350.548.

[4] D. Zhao, Q. Huo, J. Feng, B.F. Chmelka, G.D. Stucky, Nonionic triblock and star diblock copolymer and oligomeric surfactant syntheses of highly ordered, hydrothermally stable, mesoporous silica structures, J. Am. Chem. Soc. 120 (24) (1998) 6024–6036, https://doi.org/10.1021/ja974025i.

[5] S. Yuan, M. Wang, J. Liu, B. Guo, Recent advances of SBA-15-based composites as the heterogeneous catalysts in water decontamination: a mini-review, J. Environ. Manag. 254 (2020) 109787, https://doi.org/10.1016/j.jenvman.2019.109787.

[6] P. Verma, Y. Kuwahara, K. Mori, R. Raja, H. Yamashita, Functionalized mesoporous SBA-15 silica: recent trends and catalytic applications, Nanoscale 12 (21) (2020) 11333–11363, https://doi.org/10.1039/D0NR00732C.

[7] B. Jaime-Escalante, L.M. Melgoza-Contreras, G. Leyva-Gómez, N. Mendoza-Muñoz, Synthesis and drug loading improvements on mesoporous SBA-15 by spray drying, Drug. Dev. Ind. Pharm. 47 (12) (2021) 1895–1903, https://doi.org/10.1080/03639045.2022.2075009.

[8] V. Fathi Vavsari, G. Mohammadi Ziarani, A. Badiei, The Role of SBA-15 in drug delivery, RSC Adv. 5 (111) (2015) 91686–91707, https://doi.org/10.1039/C5RA17780D.

[9] X. Yan, L. Zhang, Y. Zhang, G. Yang, Z. Yan, Amine-modified SBA-15: effect of pore structure on the performance for CO_2 capture, Ind. Eng. Chem. Res. 50 (6) (2011) 3220–3226, https://doi.org/10.1021/ie101240d.

[10] I. Lacarra-Etxarri, U. De La Torre, J.A. González-Marcos, J.R. González-Velasco, B. Pereda-Ayo, Polyethylenimine-functionalized SBA-15 mesoporous silica for CO_2 direct air capture and conversion to methane in a coupled catalytic reactor, J. CO_2 Util. 97 (2025) 103134, https://doi.org/10.1016/j.jcou.2025.103134.

[11] Y.G. Ko, S.S. Shin, U.S. Choi, Primary, secondary, and tertiary amines for CO_2 capture: designing for mesoporous CO_2 adsorbents, J. Colloid Interface Sci. 361 (2) (2011) 594–602, https://doi.org/10.1016/j.jcis.2011.03.045.

[12] M. Isabel Pariente, F. Martínez, J. Ángel Botas, J. Antonio Melero, Extrusion of Fe_2O_3/SBA-15 mesoporous material for application as heterogeneous fenton-like catalyst, AIMS Environ. Sci. 2 (2) (2015) 154–168, https://doi.org/10.3934/environsci.2015.2.154.

[13] J.J. Chiu, D.J. Pine, S.T. Bishop, B.F. Chmelka, Friedel–crafts alkylation properties of aluminosilica SBA-15 meso/macroporous monoliths and mesoporous powders☆, J. Catal. 221 (2) (2004) 400–412, https://doi.org/10.1016/j.jcat.2003.09.005.

[14] A. Gupta, A.M. Choudhury, J. Meena, S. Bauri, P. Maiti, Ordered mesoporous silica delivering siRNA as cancer nanotherapeutics: a comprehensive review, ACS Biomater. Sci. Eng. 10 (5) (2024) 2636–2658, https://doi.org/10.1021/acsbiomaterials.3c01749.

[15] C. Xu, C. Lei, C. Yu, Mesoporous silica nanoparticles for protein protection and delivery, Front. Chem. 7 (2019) 290, https://doi.org/10.3389/fchem.2019.00290.

[16] L.P. Mercuri, L.V. Carvalho, F.A. Lima, C. Quayle, M.C.A. Fantini, G.S. Tanaka, W. H. Cabrera, M.F.D. Furtado, D.V. Tambourgi, J. do R. Matos, M. Jaroniec, O. A. Sant'Anna, Ordered mesoporous silica SBA-15: a new effective adjuvant to induce antibody response, Small 2 (2) (2006) 254–256, https://doi.org/10.1002/smll.200500274.

[17] C.L.P. Oliveira, J.L.S. Lopes, O.A. Sant'Anna, V.F. Botosso, H.N. Bordallo, M.C. A. Fantini, The development of new oral vaccines using porous silica, J. Phys. Condens. Matter 34 (26) (2022) 264001, https://doi.org/10.1088/1361-648X/ac6559.

[18] M.C.R. Miranda, C.M. Nunes, L.F. Santos, L.B. Da Silva, V.R. De Jesus, N.A. Filho, J. A.F. Pedro, J.L.S. Lopes, C.L.P. Oliveira, M.C.A. Fantini, J.S. Cardoso, A.G. Trezena, O.G. Ribeiro, O.A. Sant'Anna, M. Tino-De-Franco, T.S. Martins, Ordered mesoporous silicas for potential applications in solid vaccine formulations, Vaccine 42 (3) (2024) 689–700, https://doi.org/10.1016/j.vaccine.2023.12.032.

[19] M. Kozakiewicz-Latała, D. Marciniak, K. Krajewska, A. Złocińska, K. Prusik, B. Karolewicz, K.P. Nartowski, W. Pudło, Hierarchical macro-mesoporous silica monolithic tablets as a novel dose–structure-dependent delivery system for the release of confined dexketoprofen, Mol. Pharm. 20 (1) (2023) 641–649, https://doi.org/10.1021/acs.molpharmaceut.2c00834.

[20] S. Manet, J. Schmitt, M. Impéror-Clerc, V. Zholobenko, D. Durand, C.L.P. Oliveira, J.S. Pedersen, C. Gervais, N. Baccile, F. Babonneau, I. Grillo, F. Meneau, C. Rochas, Kinetics of the formation of 2D-hexagonal silica nanostructured materials by nonionic block copolymer templating in solution, J. Phys. Chem. B 115 (39) (2011) 11330–11344, https://doi.org/10.1021/jp200213k.

[21] J. Schmitt, T. Kjellman, P. Kwaśniewski, F. Meneau, J.S. Pedersen, K.J. Edler, A. R. Rennie, V. Alfredsson, M. Impéror-Clerc, Outset of the morphology of nanostructured silica particles during nucleation followed by ultrasmall-angle X-ray scattering, Langmuir 32 (20) (2016) 5162–5172, https://doi.org/10.1021/acs.langmuir.6b00572.

[22] H.I. Lee, J.H. Kim, G.D. Stucky, Y. Shi, C. Pak, J.M. Kim, Morphology-selective synthesis of mesoporous SBA-15 particles over micrometer, submicrometer and nanometer scales, J. Mater. Chem. 20 (39) (2010) 8483, https://doi.org/10.1039/c0jm00820f.

[23] R. Moulin, J. Schmitt, A. Lecchi, J. Degrouard, M. Impéror-Clerc, Morphologies of mesoporous SBA-15 particles explained by the competition between interfacial and bending energies, Soft Matter 9 (46) (2013) 11085, https://doi.org/10.1039/c3sm52108g.

[24] J. Schmitt, C. Hartwig, J.J. Crassous, A.M. Mihut, P. Schurtenberger, V. Alfredsson, Anisotropic mesoporous silica/microgel core–shell responsive particles, RSC Adv. 10 (42) (2020) 25393–25401, https://doi.org/10.1039/D0RA02278K.

[25] O. Daoura, G. Fornasieri, M. Boutros, N. El Hassan, P. Beaunier, C. Thomas, M. Selmane, A. Miche, C. Sassoye, O. Ersen, W. Baaziz, P. Massiani, A. Bleuzen, F. Launay, One-pot prepared mesoporous silica SBA-15-like monoliths with embedded ni particles as selective and stable catalysts for methane dry reforming, Appl. Catal. B Environ. 280 (2021) 119417, https://doi.org/10.1016/j.apcatb.2020.119417.

[26] N.A. Melosh, P. Davidson, B.F. Chmelka, Monolithic mesophase silica with large ordering domains, J. Am. Chem. Soc. 122 (5) (2000) 823–829, https://doi.org/10.1021/ja992801b.

[27] H. Yang, Q. Shi, B. Tian, S. Xie, F. Zhang, Yan, B. Tu, D. Zhao, A fast way for preparing crack-free mesostructured silica monolith, Chem. Mater. 15 (2) (2003) 536–541, https://doi.org/10.1021/cm020135z.

[28] R. Yildiz, Y. Lorgouilloux, J. Dhainaut, C. Ciotonea, J.-P. Dacquin, S. Royer, C. Courtois, Assembly of SBA-15 into hierarchical porous monoliths replicating polymeric scaffolds, Microporous Mesoporous Mater. 337 (2022) 111908, https://doi.org/10.1016/j.micromeso.2022.111908.

[29] A. Galarneau, Z. Abid, B. Said, Y. Didi, K. Szymanska, A. Jarzębski, F. Tancret, H. Hamaizi, A. Bengueddach, F. Di Renzo, F. Fajula, Synthesis and textural characterization of mesoporous and meso-/macroporous silica monoliths obtained by spinodal decomposition, Inorganics 4 (2) (2016) 9, https://doi.org/10.3390/inorganics4020009.

[30] J.-H. Smått, S. Schunk, M. Lindén, Versatile double-templating synthesis route to silica monoliths exhibiting a multimodal hierarchical porosity, Chem. Mater. 15 (12) (2003) 2354–2361, https://doi.org/10.1021/cm0213422.

[31] A. Galarneau, J. Iapichella, K. Bonhomme, F. Di Renzo, P. Kooyman, O. Terasaki, F. Fajula, Controlling the morphology of mesostructured silicas by pseudomorphic transformation: a route towards applications, Adv. Funct. Mater. 16 (13) (2006) 1657–1667, https://doi.org/10.1002/adfm.200500825.

[32] Y. Lakhdar, C. Tuck, J. Binner, A. Terry, R. Goodridge, Additive manufacturing of advanced ceramic materials, Progress. Mater. Sci. 116 (2021) 100736, https://doi.org/10.1016/j.pmatsci.2020.100736.

[33] A. Zocca, P. Colombo, C.M. Gomes, J. Günster, Additive manufacturing of ceramics: issues, potentialities, and opportunities, J. Am. Ceram. Soc. 98 (7) (2015) 1983–2001, https://doi.org/10.1111/jace.13700.

[34] S. Zhao, G. Siqueira, S. Drdova, D. Norris, C. Ubert, A. Bonnin, S. Galmarini, M. Ganobjak, Z. Pan, S. Brunner, G. Nyström, J. Wang, M.M. Koebel, W.J. Malfait, Additive manufacturing of silica aerogels, Nature 584 (7821) (2020) 387–392, https://doi.org/10.1038/s41586-020-2594-0.

[35] I. Cooperstein, E. Shukrun, O. Press, A. Kamyshny, S. Magdassi, Additive manufacturing of transparent silica glass from solutions, ACS Appl. Mater. Interfaces 10 (22) (2018) 18879–18885, https://doi.org/10.1021/acsami.8b03766.

[36] Q. Gu, H. Wang, W. Gao, J. Yu, X. Zhou, Preparation of large-size alumina ceramic parts by DLP 3D printing using high-solid-loading paste and optimizing the debinding process, Ceram. Int. 49 (17) (2023) 28801–28812, https://doi.org/10.1016/j.ceramint.2023.06.142.

[37] A.-K. Hofer, I. Kraleva, R. Bermejo, Additive manufacturing of highly textured alumina ceramics, Open. Ceram. 5 (2021) 100085, https://doi.org/10.1016/j.oceram.2021.100085.

[38] J. Liao, H. Chen, H. Luo, X. Wang, K. Zhou, D. Zhang, Direct ink writing of zirconia three-dimensional structures, J. Mater. Chem. C. 5 (24) (2017) 5867–5871, https://doi.org/10.1039/C7TC01545C.
[39] B. Coppola, J. Schmitt, T. Lacondemine, C. Tardivat, L. Montanaro, P. Palmero, Digital light processing stereolithography of zirconia ceramics: slurry elaboration and orientation-reliant mechanical properties, J. Eur. Ceram. Soc. 42 (6) (2022) 2974–2982, https://doi.org/10.1016/j.jeurceramsoc.2022.01.024.
[40] R. He, W. Liu, Z. Wu, D. An, M. Huang, H. Wu, Q. Jiang, X. Ji, S. Wu, Z. Xie, Fabrication of complex-shaped zirconia ceramic parts via a DLP- stereolithography-based 3D printing method, Ceram. Int. 44 (3) (2018) 3412–3416, https://doi.org/10.1016/j.ceramint.2017.11.135.
[41] B. Coppola, T. Lacondemine, C. Tardivat, L. Montanaro, P. Palmero, Designing alumina-zirconia composites by DLP-based stereolithography: microstructural tailoring and mechanical performances, Ceram. Int. 47 (10) (2021) 13457–13468, https://doi.org/10.1016/j.ceramint.2021.01.204.
[42] P. Palmero, M. Fornabaio, L. Montanaro, H. Reveron, C. Esnouf, J. Chevalier, Towards long lasting zirconia-based composites for dental implants. Part I: innovative synthesis, microstructural characterization and in vitro stability, Biomaterials 50 (2015) 38–46, https://doi.org/10.1016/j.biomaterials.2015.01.018.
[43] W. Guo, B. Li, P. Li, L. Zhao, H. You, Y. Long, Review on vat photopolymerization additive manufacturing of bioactive ceramic bone scaffolds, J. Mater. Chem. B 11 (40) (2023) 9572–9596, https://doi.org/10.1039/D3TB01236K.
[44] E. Schwarzer-Fischer, J. Abel, J. Sieder-Katzmann, M. Propst, C. Bach, U. Scheithauer, A. Michaelis, Study on CerAMfacturing of novel alumina aerospike nozzles by lithography-based ceramic vat photopolymerization (CerAM VPP), Materials 15 (9) (2022) 3279, https://doi.org/10.3390/ma15093279.
[45] G. Ding, R. He, K. Zhang, N. Zhou, H. Xu, Stereolithography 3D printing of SiC ceramic with potential for lightweight optical mirror, Ceram. Int. 46 (11) (2020) 18785–18790, https://doi.org/10.1016/j.ceramint.2020.04.196.
[46] Y. Milovanov, A. Bertero, B. Coppola, P. Palmero, J.-M. Tulliani, Mullite 3D printed humidity sensors, Ceramics 7 (2) (2024) 807–820, https://doi.org/10.3390/ceramics7020053.
[47] A. Bertero, B. Coppola, J. Schmitt, O. Gimello, P. Trens, P. Palmero, J.-M. Tulliani, 3D printed mullite monoliths with triply periodic minimal surface (TPMS) architectures functionalized with HKUST-1 for CO_2 capture, Microporous Mesoporous Mater. 390 (2025) 113601, https://doi.org/10.1016/j.micromeso.2025.113601.
[48] A. Pereira, A.F.P. Ferreira, A.E. Rodrigues, A.M. Ribeiro, M.J. Regufe, Additive manufacturing for adsorption-related applications—a review, J. Adv. Manuf. Process. 4 (1) (2022) e10108, https://doi.org/10.1002/amp2.10108.
[49] Y. Shao, Y. Yan, J. Wang, Q. Jin, H. Xu, X. Zhang, Co/SBA-16 coating supported on a 3D-printed ceramic monolith for peroxymonosulfate-activated degradation of levofloxacin, J. Colloid Interface Sci. 643 (2023) 137–150, https://doi.org/10.1016/j.jcis.2023.03.112.
[50] L.M. Schmidt, J. Dos Santos, T.V. De Oliveira, N.L. Funk, C.L. Petzhold, E. V. Benvenutti, M. Deon, R.C.R. Beck, Drug-loaded mesoporous silica on carboxymethyl cellulose hydrogel: development of innovative 3D printed hydrophilic films, Int. J. Pharm. 620 (2022) 121750, https://doi.org/10.1016/j.ijpharm.2022.121750.
[51] V. Robert, S. Loganathan, A. Sivashanmugam, S. Thomas, R.B. Valapa, 3D printed P(VdF-HFP)/SBA-15 composite-based gel polymer electrolyte versus commercial celgard: a comparative investigation on thermal stability and electrochemical performance for lithium-ion battery application, J. Am. Ceram. Soc. 107 (9) (2024) 5903–5922, https://doi.org/10.1111/jace.19863.
[52] G. Chandrasekar, M. Hartmann, V. Murugesan, Preparation of SBA-15 extrudates: evaluation of textural and mechanical properties, J. Porous Mater. 16 (2) (2009) 175–183, https://doi.org/10.1007/s10934-007-9182-7.
[53] H. Thakkar, S. Eastman, A. Al-Mamoori, A. Hajari, A.A. Rownaghi, F. Rezaei, Formulation of aminosilica adsorbents into 3D-printed monoliths and evaluation of their CO_2 capture performance, ACS Appl. Mater. Interfaces 9 (8) (2017) 7489–7498, https://doi.org/10.1021/acsami.6b16732.
[54] A. Bertero, J. Schmitt, H. Kaper, B. Coppola, P. Palmero, J.-M. Tulliani, MOFs functionalization of 3D printed mullite complex architectures for CO_2 capture, Appl. Mater. Today 40 (2024) 102407, https://doi.org/10.1016/j.apmt.2024.102407.
[55] A. Bertero, B. Coppola, Y. Milovanov, P. Palmero, J. Schmitt, J.-M. Tulliani, DLP 3D-printed mullite ceramics for the preparation of MOFs functionalized monoliths for CO_2 capture, Ceramics 7 (4) (2024) 1810–1835, https://doi.org/10.3390/ceramics7040114.
[56] O. Al-Ketan, D.-W. Lee, R. Rowshan, R.K. Abu Al-Rub, Functionally graded and multi-morphology sheet TPMS lattices: design, manufacturing, and mechanical properties, J. Mech. Behav. Biomed. Mater. 102 (2020) 103520, https://doi.org/10.1016/j.jmbbm.2019.103520.
[57] C. Hinczewski, S. Corbel, T. Chartier, Ceramic suspensions suitable for stereolithography, J. Eur. Ceram. Soc. 18 (6) (1998) 583–590, https://doi.org/10.1016/S0955-2219(97)00186-6.
[58] A. Licciulli, C. Esposito Corcione, A. Greco, V. Amicarelli, A. Maffezzoli, Laser stereolithography of ZrO2 toughened Al2O3, J. Eur. Ceram. Soc. 25 (9) (2005) 1581–1589, https://doi.org/10.1016/j.jeurceramsoc.2003.12.003.
[59] S. Manet, A. Lecchi, M. Impéror-Clerc, V. Zholobenko, D. Durand, C.L.P. Oliveira, J.S. Pedersen, I. Grillo, F. Meneau, C. Rochas, Structure of micelles of a nonionic block copolymer determined by SANS and SAXS, J. Phys. Chem. B 115 (39) (2011) 11318–11329, https://doi.org/10.1021/jp200212g.
[60] L. Ernawati, A.W. Yusariarta, R. Alviany, A. Halim, Effect of CaO/SiO_2 compositions on the structure formation of mesoporous calcium silicate ($CaSiO_3$) composite particles as adsorbent for organic dye removal, IOP Conf. Ser. Earth Environ. Sci. 963 (1) (2022) 012008, https://doi.org/10.1088/1755-1315/963/1/012008.
[61] A. Kasiri, R. Sanz, E.S. Sanz-Pérez, A. Arencibia, Amine-functionalised monolithic silica adsorbents for CO_2 capture, Environ. Sci. Adv. 4 (12) (2025) 2154–2169, https://doi.org/10.1039/D5VA00269A.
[62] Y.G. Ko, H.J. Lee, J.Y. Kim, U.S. Choi, Hierarchically porous aminosilica monolith as a CO_2 adsorbent, ACS Appl. Mater. Interfaces 6 (15) (2014) 12988–12996, https://doi.org/10.1021/am5029022.